www.sciencemag.org/content/346/6207/352/suppl/DC1

Supplementary Materials for

Ion permeation in K^+ channels occurs by direct Coulomb knock-on

David A. Köpfer, Chen Song,* Tim Gruene, George M. Sheldrick, Ulrich Zachariae,* Bert L. de Groot*

*Corresponding author. E-mail: sc3210@gmail.com (C.S.); u.zachariae@dundee.ac.uk (U.Z.); bgroot@gwdg.de (B.L.d.G.)

Published 17 October 2014, *Science* **346**, 352 (2014)
DOI: 10.1126/science.1254840

This PDF file includes:

Other supplementary material for this manuscript includes the following:

Materials and Methods

Molecular dynamics simulations

The simulation systems we used were constructed from the PDB K^+ channel crystal structures 3f5w (KcsA) (*24*), 3fb7 (KcsA) (*5*), 3ldc (MthK) and 2r9r (Kv1.2-Kv2.1 'paddle chimera', *37*). As the KcsA structure 3f5w displays the largest opening at the helix bundle gate, we used it for the majority of our simulations. We also used a computationally opened variant of the closed bundle crossing KcsA structure 1k4c as control (*38*). In the case of KcsA, the protein was protonated according to standard protonation at pH 7 except for E71, which was protonated in agreement with previous studies (*39*). The protein was inserted into a lipid bilayer surrounded by explicit water molecules and KCl. To equilibrate the system, we position-restrained all heavy atoms with a force constant of 1000 kJ mol^{-1} nm^{-2} to the reference structure (initial structure 3f5w), except for the selectivity filter motif (TTVGYG) where the high [K^+] conformation found in 1k4c (*3*) was used as a reference to create an open activated conformation. After 20 ns equilibration, the system was duplicated along the z direction and an ionic imbalance of 2 K^+ ions between the compartments was kept constant by the computational electrophysiology method (*25*), resulting in a trans-membrane voltage of approximately 200 mV. Initially, K^+ ions were positioned in the selectivity filter as found in the crystal structures (see Table S1 and S2). The control simulations were set up in an analogous way as indicated in Table S2.

We used different setups in our simulations, which varied in the lipid type (POPC or DMPC), the ion concentration, as well as the force fields, water and ion models (for details, see Table S1). Our production simulations were performed with the AMBER99sb force field (*40*). Two ion models, developed by Joung et al. and Dang et al., respectively (*41*, *42*), were utilized in our study with the AMBER99sb force field. All simulations were conducted using a modified version of Gromacs 4.6 (*43*), electrostatic interactions beyond a cutoff of 1 nm were treated by PME (*44*, *45*), and the cutoff of vdW interactions was set to 1 nm. Temperature and pressure were kept constant at 320 K and 1 bar with the v-rescale thermostat (*46*) and a semi-isotropic Berendsen barostat, respectively (*47*). All bonds were constrained with the LINCS algorithm (*48*) and virtual sites were used for protein hydrogen atoms to allow for a 4 fs integration time step (*49*). To avoid unwinding of the S6 helix, additional distance restraints were added to the backbone hydrogen bonds. To keep the cavity in an open-hydrated state, distance restraints were applied to the F103 residues as well as the ends of the S6 helix.

In addition, we also used the CHARMM36 (*50*) force field in a set of control simulations. In these simulations, instead of distance restraints, we employed restraints on the transition vector corresponding to the open-close collective motion of the helices (which was obtained from principal component analysis), to prevent the channel gates from closing. We used similar parameters as in the above AMBER simulations, with the

exceptions that the cutoff of vdW was set to 1.2 nm and a shift function was used to smoothly turn off the vdW interactions from 0.8 to 1.2 nm.

Control simulations: We carried out a number of additional control simulations as listed in Table S2.

K^+ concentration: Simulations carried out at different K^+ concentrations showed little effect on the population of the ion occupancy states in the SF (see Fig. S3). In accordance with experimental results, the current decreased as fewer ions reached the cavity per time unit. This, however, had no effect on the permeation mechanism involving direct ionic contacts we observed.

KWKW configuration: The canonical KWKW pattern in the SF most frequently leads to an impermeable state without conductance (simulations VI, VII, XIII). During some of the simulations from set VII, water was expelled from the SF, after which a sustained ionic current was recovered. All permeation events thereafter followed the reported permeation mechanism with direct ionic contacts.

Ion parameters: These simulations probed the sensitivity of our results to the employed ion model. As a variant from the most recent Joung et al. (*41*) ion parameters, we switched the parameterization to parameters according to Dang et al. (*42*) (sets VIII and IX) Both ion parameter sets were developed to more closely match experimental observables such as dehydration enthalpy. The results closely match those with the ion parameters from Joung et al.; all permeation events occurred with direct K^+–K^+ contacts and no water permeated.

Force field: Simulation sets XII and XIII were carried out using the CHARMM36 force field and with a change in the water model to TIP3P. Compared to the AMBER simulations with the SPC/E water model, two differences were observed: Firstly, the channel showed a stronger tendency to close at the lower helices, so we added an additional restraint to ensure an open conformation. Secondly, a higher transmembrane voltage of 600mV was required for ions to permeate and even then the observed currents were generally lower. The lower currents were somewhat expected as the dehydration energy of ions in CHARMM is usually larger than experimental values (*51*). However, despite these differences, all observed ion permeation events occurred with direct K^+–K^+ contacts. During sustained currents in simulation set XII no water was permeated and as in the AMBER99sb force field, adding water to the SF (as in simulation set XIII) was found to disrupt ion permeation.

Channel structure: For additional extended simulations, we used two alternative crystal

structure of KcsA: PDB id 3fb7, which is considered an open activated conformation (simulation set IX) and the closed activated structure (PDB id 1k4c), of which we used a structure that had been progressed toward the opened configuration in an extended MD simulation (*38*). In both cases, we found an identical ion permeation mechanism as in the simulations based on PDB id 3f5w (see Fig S4). In addition, we ran simulations under the same conditions using the eukaryotic Kv1.2-Kv2.1 channel chimera (PDB id 2r9r) and the high resolution MthK (PDB id 3ldc) structure used previously for our crystallographic re-refinement. Here, the overall permeation mechanism was slightly different at the level of stable configurations in the SF (e.g. in MthK S_4,S_3 and S_1 were most prominently occupied), but both channels showed continuous current (see Fig. S4) with ions in adjacent sites of the SF 'knocking-on' each other, and water was absent from the SF.

High voltage calculations: In addition, we carried out simulations with a high transmembrane voltage of ~1 V. In these simulations, the KcsA structure experiences instabilities, so a position restraint on the filter had to be applied to maintain its conformation. Interestingly, in these less realistic high-voltage simulations, K^+ and water molecules were seen to permeate in an alternating pattern.

Low temperature simulations: We carried out simulations with KcsA (PDB id: 1k4c) and MthK (PDB id: 3ldc) in water at a [K^+] of 400mM, without electrical potential and decreasing temperatures to match more closely the crystal conditions. At temperatures of 200K and below the four K^+ ions remained stably bound in the SF during the whole simulation (5 independent runs ~20ns each). With increasing temperatures up to 300K the ion occupancy included configurations closer to those observed under physiological voltages with increasing probabilities for vacancies at S_1 and S_4.

X-ray crystallography analysis

As crystallographic models represent the average of all unit cells in the crystal, the occupancy of the ion sites in crystallographic models would be less than one if water molecules were present between K^+ in the SF. In a scenario with an equal mixture of KWKW/WKWK, an effective occupancy (see eq. 1) of 0.5 would be expected for each site. In this scenario, vacancy sites instead of water molecules would result in occupancies lower than 0.5. Our analysis resulted in occupancies close to 1.0. This signifies that, in the crystal structures, K^+ ions can assume (and actually do assume) neighboring sites inside the SF. The results of all occupancy refinements are summarized in Tables S4 and S5.

Data Preparation: Data and coordinates for PDB ids 3ldc, 2qks, and 1r3j were

downloaded from www.pdb.org. Data were converted from mmCIF– to mtz–format with CIF2MTZ (*52*). The cif-file 1r3j-sf.cif contains two data blocks. The second one, r1r3jAsf, has unmerged Friedel pairs, i.e. the anomalous data. In this case CIF2MTZ was used with its subcommand "BLOCK r1r3jAsf". In case of 3ldc and 2qks, the mtz-files were converted to hkl-format with MTZ2HKL (*53*), in case of 1r3j, the mtz-file was converted to sca-format with MTZ2SCA (*53*) because of the different ways the Friedel pairs are stored in the mtz-files. Anomalous differences from 3ldc and 1r3j were extracted with XPREP (Bruker AXS, 2014). Coordinates were converted to SHELX-format with SHELXPRO (*28*). Dispersive corrections at the published wavelengths were calculated with SHELXLE (*27*) according to Kissel and Pratt (*54*), listed in Table 6. R_{free} reflections for cross validation (*55*) were conserved from the deposited data.

Refined and Effective Occupancy: According to the previous model, K^+ ions were thought unlikely to be present at adjacent sites contemporaneously. Shared ion/water occupancies were not explicitly modeled with SHELXL. Rather, the scattering from a mixture of ion/water was approximated by the scattering from the ion alone. Figure S5 displays the validity of this approximation. To quantify the minimal ion occupancy (and maximal water occupancy) in the filter, we introduce effective ion occupancies to account for the possibility that ions and water each partially occupy a binding site. In this analysis we consider a site not fully occupied with K^+ or Tl^+ to be mutually exclusively occupied with water. The effective occupancy o_{eff} shown in Tables S4 and S5 was hence calculated from the SHELXL refined occupancy o_{ref} according to

$$o_{ref} f^0(K^+) = o_{eff} f^0(K^+) + (1 - o_{eff}) f^0(H_2O)$$
$$\Leftrightarrow o_{eff} = \frac{o_{ref} f^0(K^+) - f^0(H_2O)}{f^0(K^+) - f^0(H_2O)} \qquad (1).$$

For example, for a site that is filled 50% of the time with water and 50% with a potassium ion a refined occupancy of ~0.75 would be obtained (due to the combined electron density for water and potassium), and an effective ion occupancy of 0.5. Note that if, alternatively, transient vacancies are the reason underlying partial ion occupancies (more in line with our simulation results), the effective occupancies would be identical to the reported refined occupancies. Any effective occupancies larger than 0.5 in adjacent sites are direct evidence for neighboring ions in the selectivity filter.

Refinement 1r3j: Table S7 shows the statistics for the data used for refinement of 1r3j in this study. Table S8 shows the statistics for the anomalous data of 1r3j. The PDB only stores merged data so that some quality indicators such as R_{int} or data multiplicity are not available.

The downloaded model was refined with SHELXL (*28*) without occupancy refinement for several hundred cycles to ensure convergence. After convergence, the resulting model was refined in SHELXL with individual occupancy refinement for all four Tl^+ ions. Anomalous data was taken into account in all refinement runs. Errors and correlation (Tab. S3) between parameters were calculated with SHELXL with one cycle of full-matrix least-squares refinement after removal of any restraints (*56*).
Tl^+ ions were refined anisotropically because this reduces the correlation between occupancy and U_{ij} from 0.9 to 0.8.
The refinement of 1r3j employed 13,073 restraints and 112,104 unique reflections for 17,437 parameters, i.e. a nominal data-to-parameter ratio of 7.2. 5,983 reflections were held back for cross validation. We refined the structure from R_1 = 33.7%, R_{free} = 33.7%, wR2 = 65.9% and Goof = 6.34; for the deposited structure to R_1 = 21.0%, R_{free} = 26.2%, wR2 = 45.8% and Goof = 3.38.
Note that R-values cannot be compared between different refinement programs so that the reported initial values do not match those reported in the PDB.

Refinement 3ldc: The model for 3ldc (PDB id) was refined with SHELXL analogously to 1r3j. The program ANODE (*57*) (see also below), revealed that the K^+ ion A5 at site S_{cav} in 3ldc shows no anomalous signal. It was modeled as Na^+ ion. The refinement of 3ldc employed 2,697 restraints and 27,397 unique reflections for 2,685 parameters, i.e. a nominal data-to-parameter ratio of 11.2. 3,150 reflections were held back for cross validation. We refined the structure from R_1 = 33.2%, R_{free} = 35.0%, wR2 = 69.7% and Goof = 7.29; for the deposited structure to R_1 = 22.5%, R_{free} = 25.4%, wR2 = 51.9% and Goof = 2.42. As with 1r3j, K^+ ions were refined anisotropically because this reduces the correlation between occupancy and U_{ij} from 0.9 to 0.8.

Refinement 2qks: The structure 2qks (PDB id) was refined with REFMAC5 (*58*) in addition to SHELXL. This provides results from an additional refinement method. The deposited PDB file contains so-called "LINK" records for the K^+ ions. These are distance restraints to surrounding (oxygen) atoms. Their presence leads to a deviation of the K^+ ions from their special position. After removal of the LINK records, the ions remained in the density on the four-fold symmetry axis.
The structure was refined in three rounds. The first round reset the structural model with 100 refinement cycles into convergence according to the modern refinement methods available with REFMAC5. In the second round, occupancy refinement for all K^+ ions was additionally allowed.
The refinement resulted in R = 19.0 % and R_{free} = 22.8 %. The data consist of 43990 reflections, 2180 of which were retained for R_{free} cross-validation. The resulting occupancies are listed in Table S5.
In order to see if the results are artificially connected to B-value bias, we carried out a

third round of refinement after setting the B-values of all atoms in the model to 60 Å^2, the occupancy of all four K^+ ions in the SF of chain A to 0.2 and their B-values to 30 Å^2. Those in the SF of chain B were (arbitrarily) set to 0.08 (K^+ B408), 0.16 (K^+ B409), 0.32 (K^+ B410), and 0.64 (K^+ B411) and their B-values to 30 Å^2. The results are listed in Table S5. REFMAC5 does not carry out full-matrix least-squares refinement, so that analytical standard deviations are not available. The resulting occupancies are listed in Table S5 as entry 2QKS*. Although the occupancies together with the B-values are lower, they are considerably greater than 0.5 and thus are consistent with our interpretation of the previous results.

The total number of restraints applied by REFMAC5 is 125,801. The model contains 4919 atoms which leads to 19676 parameters plus 8 parameters for the occupancies of the two times four ions in the SF. This results in a nominal data to parameter ratio of 6.4.

For comparison we also carried out refinement with SHELXL with results shown in the same table. The refinement of 2qks employed 19,768 restraints and 41,810 unique reflections for 19,521 parameters, i.e. a nominal data to parameter ratio of 3.2. 2,180 reflections were held back for cross validation. For this refinement R_1 = 24.9%, R_{free} = 30.3%, wR2 = 54.3% and Goof = 6.15. These high numbers are due to several unmodelled regions in the electron density which could be due to the detergent or other chemicals used for crystallization. The maximum likelihood method applied in REFMAC5 is more robust under these circumstances. For the SHELXL refinement, the potentially incomplete model, the relatively poor data to parameter ratio, and also the lack of anomalous data are reasons for the large variations in the figures presented in Table S5. The presented error estimates were calculated without additional restraints, so that the data to parameter ratio equals the number of unique reflections divided by the number of parameters. For the 2qks dataset this gives: 41810 / 19521 = 2.1, whereas for 1r3j this ratio equals 112104 / 17437 = 6.4, and for 3ldc we obtain 27397 / 2685 = 10.2.

Anomalous Peak Strength: ANODE (*57*) was used to calculate the anomalous peak strength in the data for 1r3j and 3ldc. They are listed in Table S9 for 1r3j and in Table S10 for 3ldc, respectively. In 3ldc the anomalous signal is weakest for S_3. Naïvely, this may be interpreted as reduced occupancy, but we would like to offer a different interpretation: If the potential well binding an ion to S_3 is less pronounced due to the nature of the oxygen atoms mimicking a hydration shell, the ion will have greater flexibility and thus fluctuate more strongly. Crystallographically this is expressed as a larger atomic displacement parameter reducing the (anomalous) signal.

The relative occupancies for 1r3j were determined with SHELXD. The input file was created with XPREP using default settings and 5000 trials.

Brownian dynamics simulations

We designed a simplified permeation model to test whether ion–ion contacts could be a more efficient permeation pattern than ion–water from a fundamental physical point of view. In this simple model, we only considered two physical interactions that are directly related to the knock-on mechanism: electrostatic and van-der-Waals interactions between the ions and water and particles interacting with an external repetitive energy potential describing a model SF. In this way, we constructed a quasi-1D system, which consists of only four K^+ ions, whose motion was restrained on the z-axis by applying two harmonic potentials ($v=0.5kr^2$, $k=3.0 \times 10^4$ kJ $mol^{-1}nm^{-2}$) on the x and y axes. An external energy potential of the form:

$$V_{ext}(z) = A \cdot \frac{\tanh(z+w) \cdot fs+1}{2} \cdot \frac{-(\tanh(z-w) \cdot fs+1)}{2} \cdot \left(\frac{1}{2}\left(\cos\left(\frac{(z-w) \cdot 2\pi \cdot p}{2w}\right)-1\right)\right) \quad ,$$

where A=15, w=0.96, p=6, fs=1.0×10^4 , was applied to K^+ to modulate the ion densities to mimic the ion distribution in the filter, as shown in Fig. 2 and S6. Then, a constant force was applied to the K^+ along the z direction to model the effect of a transmembrane voltage.

Using the above setup, we performed Brownian dynamics (BD) simulations with the HOOMD-blue software (*59*, *60*), to obtain the permeability of the ions under different constant forces (voltage). The electrostatic interaction between ions/water was described by $V_{elec}(r) = q_i q_j \frac{erfc(r_{ij})}{r_{ij}}$, and the vdW interaction was described by $V_{LJ}(r) = 4\epsilon\left[\left(\frac{\sigma}{r}\right)^{12} - \left(\frac{\sigma}{r}\right)^{6}\right]$. The vdW parameters of K^+ were set to be the same as in our MD simulations and taken from either the Dang (*42*) or Joung (*41*) parameter set. A time step of 0.01 ps was used for the BD simulations. The simulation temperature was set to 320 K. γ was set to 2720, so that K^+ had a diffusion coefficient of 0.98×10^{-9} m^2s^{-1}, about half of its value in bulk water. A dielectric constant of 1 was used for all the BD simulations.

For each applied field, six independent 1 μs simulations were performed to yield average conductance and standard deviation. We gradually increased the applied force to model transmembrane voltages increasing from 0 to 300 mV.

The same procedure was performed for two alternative systems, where in addition to four K^+, two and four water molecules were added, respectively (Fig. 2 and S6). The parameters of water were taken over from the rigid SPC/E model. γ of water oxygen and hydrogen were set to 2021 and 126, respectively, so that water had a diffusion coefficient of 1.27×10^{-9} m^2s^{-1}, about half of its value in bulk.

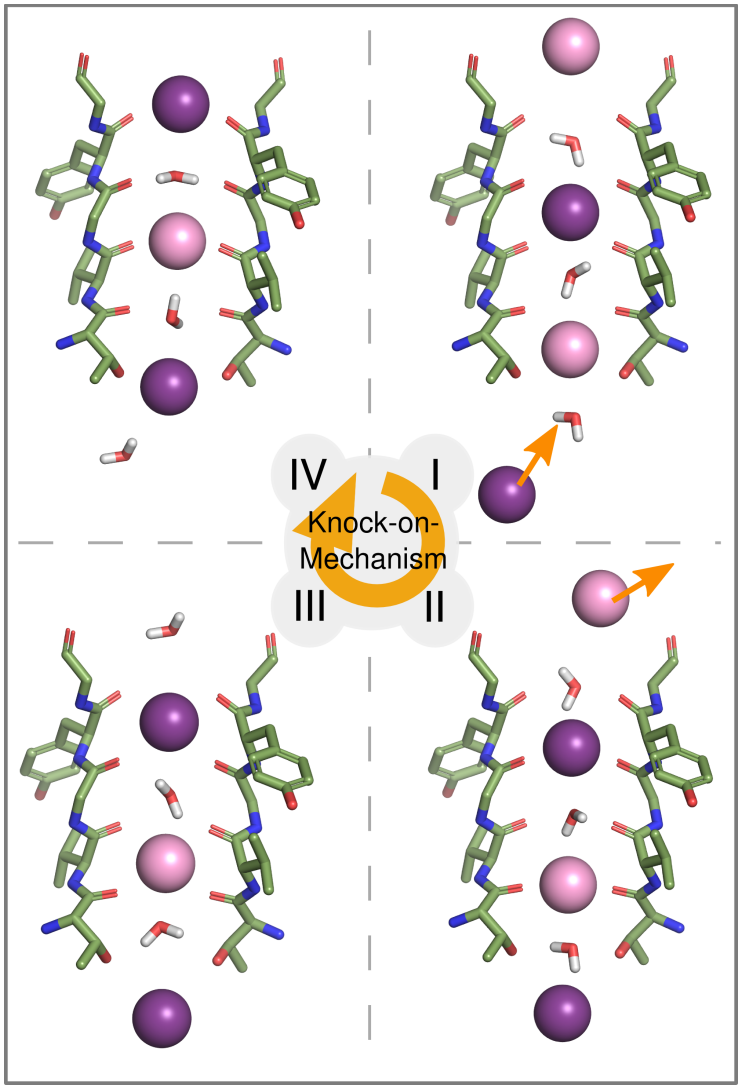

Fig. S1. The originally proposed permeation mechanism, in which K^+ and water molecules occupy the binding sites in the selectivity filter in an alternate fashion and translocate collectively (knock on). (I) K^+ ions and water molecules occupy alternating sites in the SF, in the case shown, binding sites S_2 and S_4. An arriving ion binds to S_{cav} and knocks on the column in the SF, (II) expelling the outermost ion into the bulk. (III) The SF enters its second stable conformation with ions bound to S_1 and S_3. Eventually, this conformation is thought to relax into the initial conformation, translocating a co-transported water toward the extracellular side.

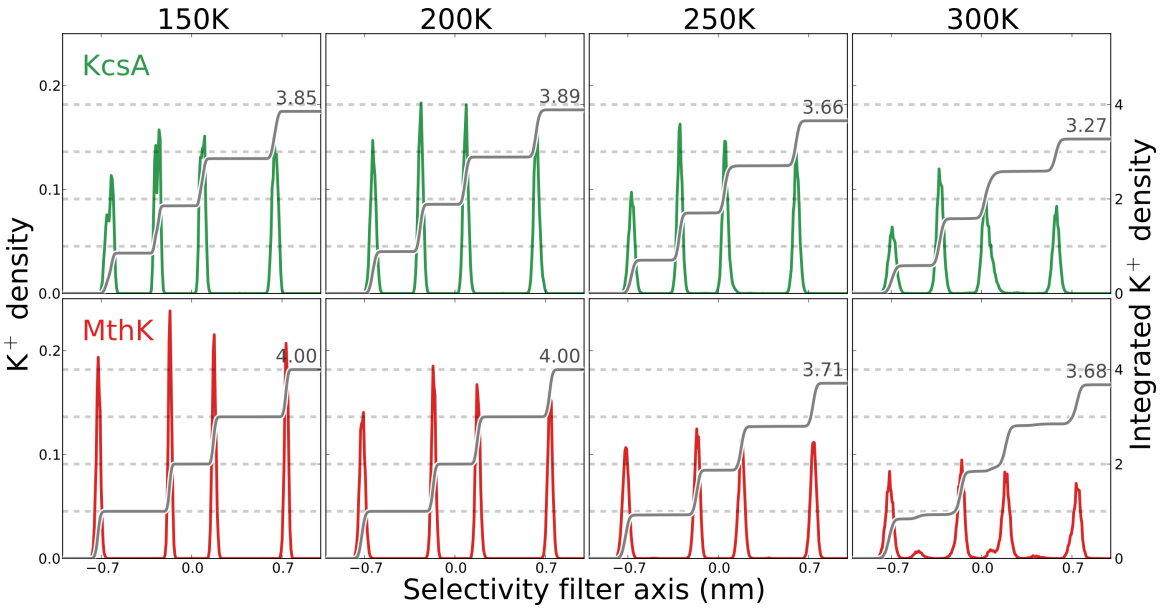

Fig. S2. K^+ ion density (KcsA: green, MthK: red; left axis) and the integration of ion density (grey lines; right axis) along the selectivity filter axis at different temperatures from MD simulations. In the low temperature regime (i.e. ≤ 200 K, at crystallization conditions), 4 K^+ ions stably bind to the SF of the K^+ channels at a [K^+] of 400 mM, while an increase in temperature to physiological conditions recovers ionic configurations found in conductive channels during production simulations.

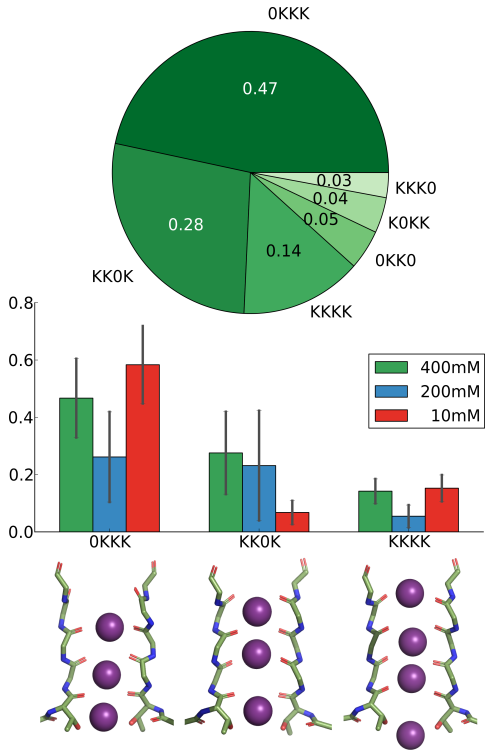

Fig. S3. Population of ionic configuration states in the selectivity filter. Top panel: Pie chart of all observed states with a population > 0.02 in KcsA simulations of set I (~400mM; ~200mV), the naming of states corresponds to K^+ ion binding at sites S_1 through S_4, 0 denotes a vacancy. Middle panel: Population distribution as a function of concentration of the three most populated states. The majority of states contain direct ion-ion contacts under all investigated concentrations. Bottom panel: Representative SF snapshots of the three most populated states. Independent of the ion concentration the two most populated states account for about 60 % of all ion configurations. The lower current due to the smaller number of ions arriving at the cavity at lower ion concentrations explains the increasing trend of 0KKK and decreasing trend of KK0K with reduced concentration.

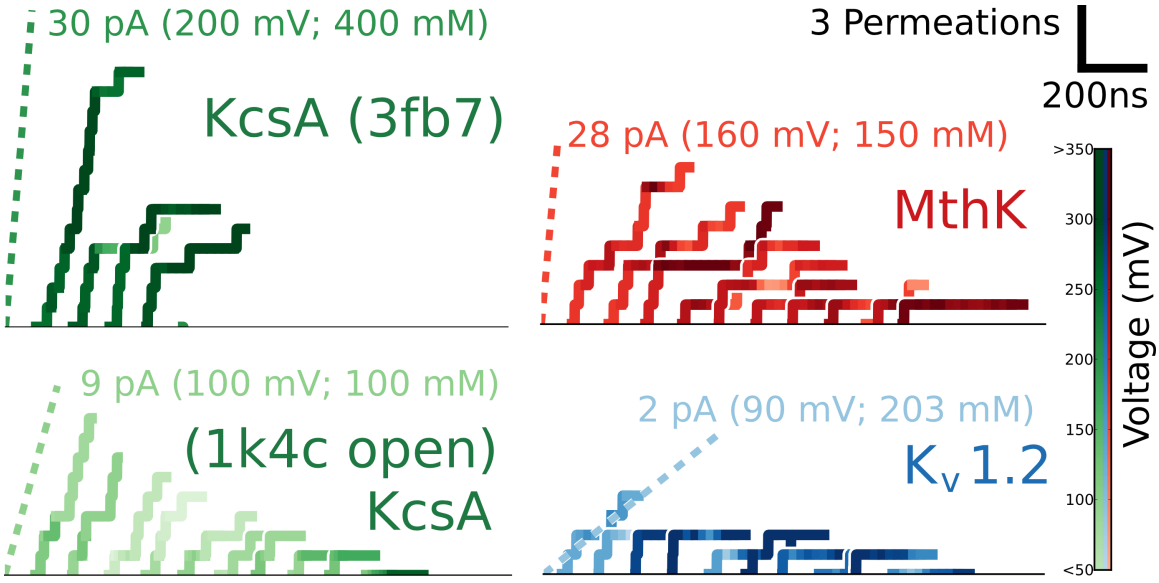

Fig. S4. Permeation events as a function of time for different K^+ channels. Simulations of KcsA (green) started form the crystal structure PDB id 3fb7 (top left, simulation set IX) and a conductive form of PDB id 1k4c that had previously been driven toward an opened state at the bundle crossing in an MD simulation using essential dynamics (*39*) (bottom left, simulation set XIV). The reported experimental current is displayed as dashed lines (*36*). Simulations of the archaeal MthK channel PDB id 3ldc (red, top right, simulation set XV, experimental currents *61*) and the eukaryotic $K_v1.2$ channel variant PDB id 2r9r (blue, bottom right, simulation set XVI, experimental currents *62*). Each step represents the permeation of a single K^+ ion, the transmembrane voltage recorded in experiments or simulations is color–coded as shown in the color bar on the right.

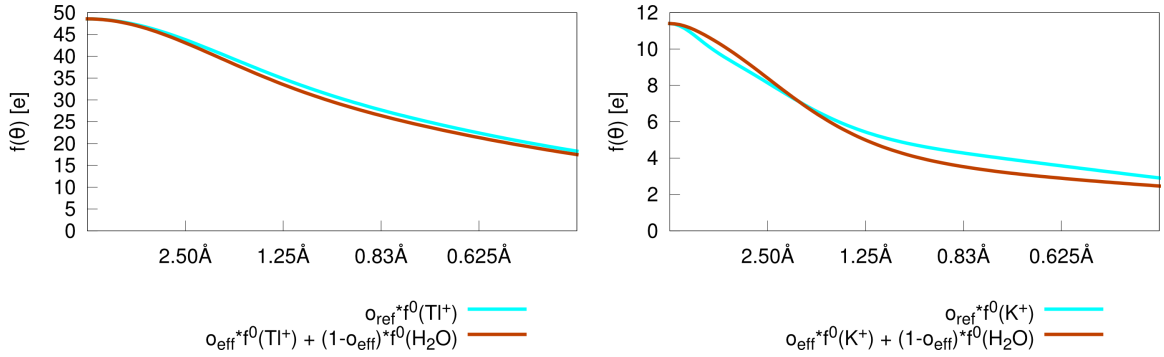

Fig. S5. The scattering factor from either K^+ or Tl^+ compared to a mixture of H_2O and ion with an exemplary occupancy o_{ref} = 0.6. The difference is only small and justifies the modeling in the crystal structure with an ion only instead of using a mixed state. The latter leads to an unstable refinement.

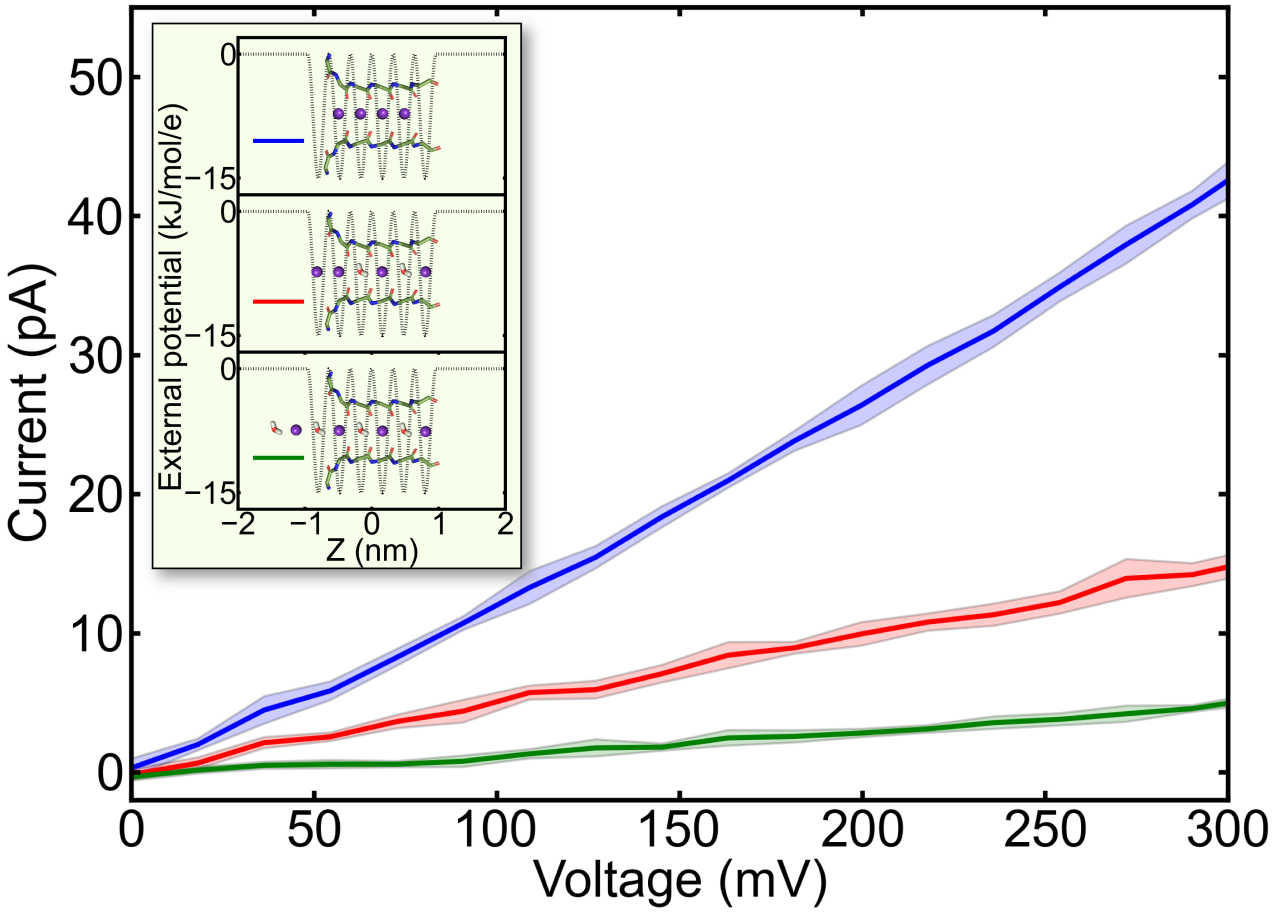

Fig. S6. Control Brownian dynamics simulation with ion parameters taken from Dang et al. (*42*). Qualitatively, the same results were obtained as in Fig. 2, where Joung et al. parameters were used (*41*). Direct ion contacts lead to the highest conductance while the presence of water molecules suppresses conduction.

Table S1. Simulation details for production MD simulations. Production simulations (I-V) varied in lipid composition and ion concentration.

	Production				
Simulation set	**I**	**II**	**III**	**IV**	**V**
Structure	KcsA 3f5w with 1k4c SF	KcsA 3f5w with 1k4c SF	KcsA 3f5w with 1k4c SF	KcsA 3f5w with 1k4c SF	KcsA 3f5w with 1k4c SF
force field	amber99sb	amber99sb	amber99sb	amber99sb	amber99sb
Lipid	432 **POPC** Berger et al.	432 **POPC** Berger et al.	432 **POPC** Berger et al.	356 **DMPC** Berger et al.	356 **DMPC** Berger et al.
Water	29052 SPC/E	29610 SPC/E	29610 SPC/E	18272 SPC/E	18272 SPC/E
Ion	**400mM** 312 K^+ 320 Cl^- Joung et al.	**200mM** 190 K^+ 198 Cl^- Joung et al.	**10mM** 15 K^+ 23 Cl^- Joung et al.	**400mM** 230 K^+ 238 Cl^- Joung et al.	**200mM** 116 K^+ 124 Cl^- Joung et al.
SF starting pattern ($S_0 - S_{cav}$)	KKKKKK	KKKKKK	KKKKKK	KKKKKK	KKKKKK
Independent simulations	20	15	10	10	10
Total simulation time (μs)	15.1	4.1	4.7	5.1	2.7
Total permeations	496	136	28	267	83
Voltage (mV)	210±70	230±80	260±20	370±140	440±110

Table S2. Simulation details for production MD simulations. For control simulations (VI-XVI), the major modifications compared to the production simulations are indicated in bold face.

						Control					
Simulation set	**VI**	**VII**	**VIII**	**IX**	**X**	**XI**	**XII**	**XIII**	**XIV**	**XV**	**XVI**
Structure	KcsA 3f5w with 1k4c SF	KcsA 3f5w with 1k4c SF	KcsA 3f5w with 1k4c SF	KcsA **3fb7**	KcsA 3f5w with 1k4c SF	KcsA 3f5w with 1k4c SF	KcsA 3f5w with 1k4c SF	KcsA 3f5w with 1k4c SF	KcsA **1k4c** with opened gate	**MthK 3ldc**	**Kv1.2 2r9r** with 1k4c SF
force field	amber99sb	amber99sb	amber99sb	amber99sb	amber99sb	amber99sb	**charmm36**	**charmm36**	amber99sb	amber99sb	amber99sb
Lipid	356 DMPC Berger et al.	432 POPC Berger et al.	356 DMPC Berger et al.	398 DMPC Berger et al.	432 POPC Berger et al.	432 POPC Berger et al.	378 DMPC charmm	378 DMPC charmm	428 DMPC Berger et al.	432 POPC Berger et al.	POPC Berger et al.
Water	18272 SPC/E	29052 SPC/E	18272 SPC/E	25120 SPC/E	29052 **TIP3P**	29052 **TIP4P**	20892 **TIP3P**	20892 **TIP3P**	29678 SPC/E	28693 SPC/E	24688 SPC/E
Ion	400mM 230 K^+ 238 Cl^- Joung et al.	400mM 312 K^+ 320 Cl^- Joung et al.	400 mM 230 K^+ 238 Cl^- **Dang et al.**	600mM 470 K^+ 486 Cl^- **Dang et al.**	400mM 312 K^+ 320 Cl^- Joung et al.	400mM 312 K^+ 320 Cl^- Joung et al.	400 mM 270 K^+ 278 Cl^- **charmm36**	400 mM 270 K^+ 278 Cl^- **charmm36**	100 mM 148 K^+ 148 Cl^- Joung et al.	300mM 311 K^+ 287 Cl^- Joung et al.	600mM 470 K^+ 454 Cl^- Joung et al.
SF starting pattern ($S_0 - S_{cav}$)	**WKWKWK**	**WKWKWK**	KKKKKK	KKKKKK	KKKKKK	KKKKKK	KKKKKK	**WKWKWK**	KKKKKK	KKKKKK	KKKKKK
Independent simulations	4	6	5	5	5	5	5	5	10	10	10
Total simulation time (μs)	1.1	1.4	1.5	1.7	1.2	1.0	1.0	1.3	1.7	3.9	2.5
Total permeations	0	31*	70	27	80	42	29	0	33	39	21
Voltage (mV)	210±70	180±70	220±40	240±90	200±80	370±60	560±120	340±66	90±50	220±60	230±120

*all permeation events occurred after direct ionic contacts were recovered.

Table S3. Correlation between the occupancy and atomic displacement parameters for the SF ions in PDB structures 1r3j and 3ldc, calculated with full matrix refinement in SHELXL. Despite somewhat lower resolution, 1r3j shows better agreement between anisotropic and isotropic refinement with smaller correlation coefficients. Owing to the I4 symmetry, only the diagonal elements of U are non-zero in the anisotropic refinement, and U_{22}=U_{11}. For 1r3j, correlations between occupancy and U_{33} below 0.72 were not specified further, as SHELXL only lists the 600 strongest correlations.

PDB id: 1r3j		**anisotropic refinement**					**isotropic refinement**		
Atom	**binding site**	**occupancy**	**U_{11}/U_{22}**	**U_{33}**	**occ. correlation with U_{11}**	**occ. correlation with U_{33}**	**occupancy**	**correlation**	**U_{iso}**
TL1	S_1	1.02	0.395	0.281	0.809	< 0.72	1.01	0.895	0.358
TL2	S_2	0.93	0.376	0.219	0.812	0.731	0.92	0.896	0.325
TL3	S_3	0.92	0.346	0.260	0.816	< 0.72	0.90	0.898	0.307
TL4	S_4	0.99	0.405	0.229	0.807	< 0.72	0.98	0.901	0.342

PDB id: 3ldc		**anisotropic refinement**					**isotropic refinement**		
Atom	**binding site**	**occupancy**	**U_{11}/U_{22}**	**U_{33}**	**occ. correlation with U_{11}**	**occ. correlation with U_{33}**	**occupancy**	**correlation**	**U_{iso}**
K1	S_1	0.91	0.223	0.237	0.841	0.706	0.87	0.919	0.221
K2	S_2	0.78	0.238	0.138	0.830	0.792	0.84	0.925	0.212
K3	S_3	1.22	0.257	0.284	0.835	0.695	1.15	0.915	0.258
K4	S_4	1.10	0.242	0.322	0.842	0.644	1.07	0.911	0.263

Table S4: Results for occupancy refinement of Tl^+ in PDB id 1r3j and K^+ in PDB id 3ldc, respectively. Standard uncertainties are given where available (SHELXL refinement); "n/a" means that the anomalous signal was too weak for reliable calculation. (Occupancies greater than one are caused by the correlation between occupancies and B-values.) U_{ij} values from SHELXL (1r3j, 3ldc) were converted by the standard conversions $B_{iso} = 8\pi^2/3\ (U_{xx}+U_{yy}+U_{zz})$ and $s_{iso} = 8\pi^2/3\ (\sigma_{xx} + \sigma_{yy} + \sigma_{zz})$. Please see main text and Eq. 1 for a definition of occ_{ref} and occ_{eff}.

	SHELXL			
1r3j	**TL^+ C401**	**TL^+ C402**	**TL^+ C403**	**TL^+ C404**
rel. occ	1.0	0.9	0.9	1.0
abs. occ_{ref}	1.02 (4)	0.93 (3)	0.92 (4)	0.99 (4)
abs. occ_{eff}	1.02 (5)	0.92 (3)	0.91 (5)	0.99 (5)
B[Å²]	22(1)	26(1)	25(1)	20(2)
	SHELXL			
3ldc	**K^+ A1**	**K^+ A2**	**K^+ A3**	**K^+ A4**
rel. occ.	n/a	n/a	n/a	n/a
abs. occ_{ref}	0.92 (7)	0.80 (7)	1.00 (8)	1.00 (8)
abs. occ_{eff}	0.81(16)	0.57(15)	1.00(16)	1.00(17)
B[Å²]	18(1)	17(1)	18(1)	20(1)

Table S5: Results for occupancy refinement of K^+ in PDB id 2qks from REFMAC5 and SHELX, respectively. Standard uncertainties given where available (SHELXL refinement). Occupancies greater than one are caused by the correlation between occupancies and B-values. 2qks denotes the refinement of the deposited PDB parameters, 2qks* denotes the refinement after resetting B and occupancy as described in the text. U_{ij} values from SHELXL (1r3j, 3ldc) were converted by the standard conversions $B_{iso} = 8\pi^2/3\ (U_{xx} + U_{yy} + U_{zz})$ and $s_{iso} = 8\pi^2/3\ (\sigma_{xx} + \sigma_{yy} + \sigma_{zz})$. Refer to text and Eq. 1 for occ_{ref} and occ_{eff}.

REFMAC 5

2qks	**K^+ A401**	**K^+ A402**	**K^+ A403**	**K^+ A404**	**K^+ B408**	**K^+ B409**	**K^+ B410**	**K^+ B411**
abs. occ_{ref}	1.00	1.00	1.00	0.92	0.96	0.92	0.96	0.68
abs. occ_{eff}	1.00	1.00	1.00	0.83	0.92	0.83	0.92	0.32
B[Å^2]	33.7	31.8	38.2	60.5	38.7	31.0	40.6	38.7
2qks*	**K^+ A401**	**K^+ A402**	**K^+ A403**	**K^+ A404**	**K^+ B408**	**K^+ B409**	**K^+ B410**	**K^+ B411**
abs. occ_{ref}	1.00	0.96	1.00	0.84	0.88	0.76	0.80	0.80
abs. occ_{eff}	1.00	0.92	1.00	0.66	0.75	0.49	0.58	0.58
B[Å^2]	33.9	30.7	38.5	49.9	34.1	26.6	33.8	56.1

SHELXL

2qks	**K^+ A401**	**K^+ A402**	**K^+ A403**	**K^+ A404**	**K^+ B408**	**K^+ B409**	**K^+ B410**	**K^+ B411**
abs. occ_{ref}	1.0(3)	1.0(4)	1.0(4)	0.5(3)	1.0(4)	0.8(4)	0.9(4)	0.6(3)
abs. occ_{eff}	1.0(6)	1.0(8)	1.0(8)	0.0(6)	1.0(8)	0.6(8)	0.8(8)	0.2(6)
B[Å^2]	34(13)	37(14)	42(13)	42(21)	42(19)	39(21)	46(17)	51(22)
2qks*	**K^+ A401**	**K^+ A402**	**K^+ A403**	**K^+ A404**	**K^+ B408**	**K^+ B409**	**K^+ B410**	**K^+ B411**
abs. occ_{ref}	1.0(7)	1.0(7)	1.0(6)	0.7(5)	1.0(9)	1.0(9)	1.0(7)	0.9(5)
abs. occ_{eff}	1.0(1.5)	1.0(1.5)	1.0(1.3)	0.4(1.1)	1.0(1.9)	1.0(1.9)	1.0(1.5)	0.8(1.0)
B[Å^2]	50(32)	50(32)	50(26)	50(27)	54(41)	54(41)	54(32)	55(55)

Table S6: Calculated dispersive corrections f′(λ) and f′′(λ) for K^+ and Tl^+. Dispersive corrections for all other elements were taken into account but only those for *S* differ significantly from 0*e* (*27*, *54*).

	1r3j (λ = 0.9504 Å)		**3ldc (λ = 0.9794 Å)**	
	Tl	**S**	**K**	**S**
***f′*[e]**	-8.965	0.195	0.298	0.203
***f″*[e]**	9.678	0.224	0.469	0.238

Table S7: Data statistics for the dataset 1r3j, data block r1r3jAsf, as deposited in the PDB. Res: Resolution shell; #data: measured number of reflections; #pred: theoretically possible number of reflections; %compl: data completeness, *i.e.* %compl = 100% × #data/#pred. Statistics are from XPREP

Res. [Å]	# data	# pred.	% compl.	$\langle I/\sigma_I \rangle$
∞ – **8.04**	919	1006	91.4	27.80
8.04 – 5.43	2150	2156	99.7	27.12
5.43 – 4.32	3037	3040	99.9	27.65
4.32 – 3.77	3068	3068	100.0	26.15
3.77 – 3.42	3112	3112	100.0	23.85
3.42 – 3.18	2974	2975	100.0	21.01
3.18 – 2.99	3106	3106	100.0	18.82
2.99 – 2.84	3040	3041	100.0	16.01
2.84 – 2.71	3221	3221	100.0	13.46
2.71 – 2.61	2910	2911	100.0	13.27
2.61 – 2.52	3031	3039	99.7	11.52
2.52 – 2.44	3092	3096	99.9	9.89
2.44 – 2.37	3045	3051	99.8	8.60
2.37 – 2.30	3437	3445	99.8	7.68
2.30 – 2.25	2705	2711	99.8	6.63
2.25 – 2.20	2968	2982	99.5	6.02
2.20 – 2.15	3242	3249	99.8	5.50
2.15 – 2.10	3574	3591	99.5	4.99
2.10 – 2.06	3071	3092	99.3	4.15
2.06 – 2.03	2446	2468	99.1	3.84
2.03 – 2.00	2900	2938	98.7	3.19
2.10 – 2.00	8417	8498	99.0	3.73
∞ – **2.00**	61048	61292	99.6	13.02

Table S8: Data statistics for the anomalous differences from 1r3j used for determination of the relative occupancies with SHELXD. Res: Resolution shell; #data: measured number of reflections; #pred: theoretically possible number of differences; %compl: data completeness, *i.e.* %compl = 100% × #data/#pred. Statistics are from XPREP

Res. [Å]	# data	# pred.	% compl.	$\langle I/\sigma_I \rangle$
∞ – **7.80**	857	1088	78.8	2.93
7.80 – 5.37	1992	2187	91.1	2.92
5.37 – 4.29	2860	3054	93.6	2.45
4.29 – 3.76	2869	3022	94.9	2.30
3.76 – 3.42	2889	3031	95.3	2.42
3.42 – 3.18	2835	2975	95.3	2.59
3.18 – 3.00	2789	2918	95.6	2.60
3.00 – 2.85	2890	3005	96.2	2.68
2.85 – 2.73	2777	2886	96.2	2.52
2.73 – 2.62	3019	3148	95.9	2.56
2.62 – 2.53	2854	3006	94.9	2.50
2.53 – 2.45	2885	3045	94.7	2.24
2.45 – 2.38	2816	3007	93.6	2.19
2.38 – 2.31	3130	3376	92.7	2.13
2.31 – 2.26	2466	2672	92.3	2.01
2.26 – 2.20	3251	3540	91.8	1.99
2.20 – 2.16	2359	2587	91.2	1.93
2.16 – 2.11	3127	3475	90.0	1.86
2.11 – 2.07	2749	3055	90.0	1.83
2.07 – 2.03	2922	3283	89.0	1.73
2.03 – 2.00	2557	2938	87.0	1.65
2.10 – 2.00	7528	8498	88.6	1.73
∞ – **2.00**	56893	61292	92.8	2.26

Table S9: Anomalous peak density for all four Tl^+ ions in 1r3j. There are no peaks near S atoms above the noise level of about 5σ. The height is measured in standard deviations σ of the map. Δ_{peak} denotes the distance between the peak and the respective ion.

	S_1	S_2	S_3	S_4
σ	86.1	85.3	83.3	82.1
Δ_{peak} [Å]	0.01	0.02	0.01	0.03

Table S10: Anomalous peak density for all four K^+ ions in 3ldc. The two highest S peaks are included for comparison. The height is measured in standard deviations σ of the map. Δ_{peak} denotes the distance between the peak and the respective ion/atom.

	S_1	S_2	S_3	S_4	S_δ(Met73)	S_γ(Cys77)
σ	18.7	16.7	14.2	19.3	7.8	6.9
Δ_{peak}[Å]	0.09	0.01	0.23	0.09	0.09	0.23

Table S11: Data statistics for the data set 2qks as deposited in the PDB. Res: Resolution shell;#data: measured number of reflections; #pred: theoretically possible number of reflections; %compl: data completeness, i.e. %compl = 100% × #data / #pred. Statistics are from XPREP.

Res. [Å]	# data	# pred.	% compl.	$\langle I/\sigma_I \rangle$
∞ – 8.14	666	941	70.8	33.63
8.14 – 5.77	1550	1632	95.0	33.21
5.77 – 4.65	2190	2281	96.0	31.71
4.65 – 4.08	2233	2311	96.6	32.18
4.08 – 3.72	2211	2269	97.4	29.81
3.72 – 3.46	2183	2238	97.5	27.40
3.46 – 3.26	2241	2288	97.9	24.21
3.26 – 3.10	2173	2219	97.9	21.32
3.10 – 2.97	2172	2210	98.3	18.42
2.97 – 2.85	2372	2410	98.4	16.46
2.85 – 2.76	2048	2077	98.6	13.82
2.76 – 2.67	2347	2376	98.8	12.16
2.67 – 2.60	2041	2056	99.3	10.07
2.60 – 2.53	2309	2323	99.4	8.91
2.53 – 2.47	2201	2208	99.7	7.65
2.47 – 2.41	2389	2400	99.5	6.60
2.41 – 2.36	2216	2223	99.7	5.60
2.36 – 2.32	1875	1879	99.8	5.09
2.32 – 2.27	2594	2600	99.8	4.51
2.27 – 2.23	2209	2212	99.9	3.87
2.23 – 2.20	1770	1814	97.6	3.42
2.30 – 2.20	5548	5597	99.1	3.88
∞ – 2.20	43990	44962	97.8	15.90

Table S12: Estimate of the strength of the anomalous signal in 1r3j. The signal is considered significant up to $\Delta F_{ano}/\sigma_{anp} > 1.3$ (*63*)

d [Å]	∞	-8.0	-6.0	-5.0	-4.0	-3.5	-3.2	-3.0	-2.8	-2.6	-2.4	-2.2	-2.0
$\mathbf{\Delta F_{ano}/\sigma_{ano}}$		1.64	1.56	1.54	1.25	1.33	1.50	1.49	1.54	1.44	1.33	1.21	1.07

Table S13: Data statistics for the data set 3ldc as deposited in the PDB. Res: Resolution shell; #data: measured number of reflections ; #pred: theoretically possible number of reflections; %compl: data completeness, i.e. %compl = 100 % x #data / #pred. Statistics are from XPREP.

Res. [Å]	# data	# pred.	% compl.	$\langle I/\sigma I \rangle$
∞ – 5.70	250	343	72.9	63.24
5.70 – 3.95	581	606	95.9	72.69
3.95 – 3.15	834	836	99.8	71.59
3.15 – 2.75	840	842	99.8	60.73
2.75 – 2.50	821	822	99.9	55.80
2.50 – 2.32	829	830	99.9	47.22
2.32 – 2.18	837	838	99.9	42.36
2.18 – 2.07	821	821	100.0	35.54
2.07 – 1.98	814	815	99.9	30.83
1.98 – 1.90	863	864	99.9	25.13
1.90 – 1.83	867	867	100.0	18.59
1.83 – 1.77	854	855	99.9	14.15
1.77 – 1.72	816	817	99.9	11.38
1.72 – 1.67	931	931	100.0	8.18
1.67 – 1.63	792	793	99.9	6.72
1.63 – 1.59	894	894	100.0	5.58
1.59 – 1.56	729	729	100.0	4.49
1.56 – 1.53	784	785	99.9	3.56
1.53 – 1.50	847	847	100.0	3.18
1.50 – 1.47	914	915	99.9	2.39
1.47 – 1.45	644	659	97.7	1.84
1.55 – 1.45	2943	2959	99.5	2.72
∞ – 1.45	16562	16708	99.1	26.13

Table S14: Data statistics for the anomalous differences extracted from 3ldc. Res: Resolution shell; #data: measured number of reflections; #pred: theoretically possible number of reflections; %compl: data completeness, i.e. %compl = 100 % x #data / #pred. Statistics are from XPREP.

Res. [Å]	# data	# pred.	% compl.	$\langle I/\sigma I \rangle$
∞ – 5.32	182	413	44.1	1.29
5.32 – 3.81	427	636	67.1	0.99
3.81 – 3.12	605	785	77.1	1.19
3.12 – 2.76	609	762	79.9	1.25
2.76 – 2.53	607	744	81.6	1.23
2.53 – 2.36	601	731	82.2	1.26
2.36 – 2.23	599	720	83.2	1.12
2.23 – 2.12	637	762	83.6	1.06
2.12 – 2.03	623	744	83.7	1.02
2.03 – 1.96	561	665	84.4	0.92
1.96 – 1.89	646	769	84.0	0.99
1.89 – 1.83	604	753	80.2	0.89
1.83 – 1.78	559	715	78.2	0.87
1.78 – 1.73	612	794	77.1	0.93
1.73 – 1.68	675	880	76.7	0.91
1.68 – 1.64	564	790	71.4	0.89
1.64 – 1.60	628	877	71.6	0.77
1.60 – 1.56	644	963	66.9	0.84
1.56 – 1.53	483	785	61.5	0.84
1.53 – 1.49	639	1146	55.8	0.75
1.49 – 1.45	575	1267	45.4	0.76
1.55 – 1.45	1540	2951	52.2	0.77
∞ – 1.45	12080	16700	72.3	0.98

Movie S1: K^+ ion permeation within a 50-ns trajectory from our computational electrophysiology molecular dynamics simulations. For clarity, only two subunits of KcsA are shown. K^+ ions are shown as purple spheres. As can be seen from the movie, the knock-on permeation mechanism in the K^+ channel is based on close contacts between adjacent K^+ ions in the filter, and water molecules are not directly involved in the permeation process under physiological transmembrane voltage (<250 mV in our simulations), even though water is able to access site S_4 occasionally.

References

1. B. Hille, *Ion Channels of Excitable Membranes* (Sinauer, Sunderland, MA, ed. 3, 2001).

2. D. A. Doyle, J. Morais Cabral, R. A. Pfuetzner, A. Kuo, J. M. Gulbis, S. L. Cohen, B. T. Chait, R. MacKinnon, The structure of the potassium channel: Molecular basis of K^+ conduction and selectivity. *Science* **280**, 69–77 (1998). Medline doi:10.1126/science.280.5360.69

3. Y. Zhou, J. H. Morais-Cabral, A. Kaufman, R. MacKinnon, Chemistry of ion coordination and hydration revealed by a K^+ channel-Fab complex at 2.0 A resolution. *Nature* **414**, 43–48 (2001). Medline doi:10.1038/35102009

4. Y. Zhou, R. MacKinnon, The occupancy of ions in the K^+ selectivity filter: Charge balance and coupling of ion binding to a protein conformational change underlie high conduction rates. *J. Mol. Biol.* **333**, 965–975 (2003). Medline doi:10.1016/j.jmb.2003.09.022

5. L. G. Cuello, V. Jogini, D. M. Cortes, A. C. Pan, D. G. Gagnon, O. Dalmas, J. F. Cordero-Morales, S. Chakrapani, B. Roux, E. Perozo, Structural basis for the coupling between activation and inactivation gates in K^+ channels. *Nature* **466**, 272–275 (2010). Medline doi:10.1038/nature09136

6. C. Domene, M. S. P. Sansom, Potassium channel, ions, and water: Simulation studies based on the high resolution X-ray structure of KcsA. *Biophys. J.* **85**, 2787–2800 (2003). Medline doi:10.1016/S0006-3495(03)74702-X

7. A. L. Hodgkin, R. D. Keynes, The potassium permeability of a giant nerve fibre. *J. Physiol.* **128**, 61–88 (1955). Medline

8. C. Miller, See potassium run. *Nature* **414**, 23–24 (2001). Medline doi:10.1038/35102126

9. J. H. Morais-Cabral, Y. Zhou, R. MacKinnon, Energetic optimization of ion conduction rate by the K^+ selectivity filter. *Nature* **414**, 37–42 (2001). Medline doi:10.1038/35102000

10. J. Åqvist, V. Luzhkov, Ion permeation mechanism of the potassium channel. *Nature* **404**, 881–884 (2000). Medline doi:10.1038/35009114

11. L. Ceccarini, M. Masetti, A. Cavalli, M. Recanatini, Ion conduction through the hERG potassium channel. *PLOS ONE* **7**, e49017 (2012). Medline doi:10.1371/journal.pone.0049017

12. F. Khalili-Araghi, E. Tajkhorshid, K. Schulten, Dynamics of K^+ ion conduction through Kv1.2. *Biophys. J.* **91**, L72–L74 (2006). Medline doi:10.1529/biophysj.106.091926

13. G. Yellen, The voltage-gated potassium channels and their relatives. *Nature* **419**, 35–42 (2002). Medline doi:10.1038/nature00978

14. T. Lu, A. Y. Ting, J. Mainland, L. Y. Jan, P. G. Schultz, J. Yang, Probing ion permeation and gating in a K^+ channel with backbone mutations in the selectivity filter. *Nat. Neurosci.* **4**, 239–246 (2001). Medline doi:10.1038/85080

15. S. Bernèche, B. Roux, Molecular dynamics of the KcsA K^+ channel in a bilayer membrane. *Biophys. J.* **78**, 2900–2917 (2000). Medline doi:10.1016/S0006-3495(00)76831-7

16. I. H. Shrivastava, M. S. P. Sansom, Simulations of ion permeation through a potassium channel: Molecular dynamics of KcsA in a phospholipid bilayer. *Biophys. J.* **78**, 557–570 (2000). Medline doi:10.1016/S0006-3495(00)76616-1

17. T. Sumikama, S. Saito, I. Ohmine, Mechanism of ion permeation in a model channel: Free energy surface and dynamics of K^+ ion transport in an anion-doped carbon nanotube. *J. Phys. Chem. B* **110**, 20671–20677 (2006). Medline doi:10.1021/jp062547r

18. S. Bernèche, B. Roux, Energetics of ion conduction through the K^+ channel. *Nature* **414**, 73–77 (2001). Medline doi:10.1038/35102067

19. M. Ø. Jensen, D. W. Borhani, K. Lindorff-Larsen, P. Maragakis, V. Jogini, M. P. Eastwood, R. O. Dror, D. E. Shaw, Principles of conduction and hydrophobic gating in K^+ channels. *Proc. Natl. Acad. Sci. U.S.A.* **107**, 5833–5838 (2010). Medline doi:10.1073/pnas.0911691107

20. M. Ø. Jensen, V. Jogini, M. P. Eastwood, D. E. Shaw, Atomic-level simulation of current-voltage relationships in single-file ion channels. *J. Gen. Physiol.* **141**, 619–632 (2013). Medline doi:10.1085/jgp.201210820

21. K. Kasahara, M. Shirota, K. Kinoshita, Ion concentration-dependent ion conduction mechanism of a voltage-sensitive potassium channel. *PLOS ONE* **8**, e56342 (2013). Medline doi:10.1371/journal.pone.0056342

22. S. Furini, C. Domene, Atypical mechanism of conduction in potassium channels. *Proc. Natl. Acad. Sci. U.S.A.* **106**, 16074–16077 (2009). Medline doi:10.1073/pnas.0903226106

23. P. W. Fowler, E. Abad, O. Beckstein, M. S. P. Sansom, Energetics of multi-ion conduction pathways in potassium ion channels. *J. Chem. Theory Comput.* **9**, 5176–5189 (2013). Medline doi:10.1021/ct4005933

24. L. G. Cuello, V. Jogini, D. M. Cortes, E. Perozo, Structural mechanism of C-type inactivation in K^+ channels. *Nature* **466**, 203–208 (2010). Medline doi:10.1038/nature09153

25. C. Kutzner, H. Grubmüller, B. L. de Groot, U. Zachariae, Computational electrophysiology: The molecular dynamics of ion channel permeation and selectivity in atomistic detail. *Biophys. J.* **101**, 809–817 (2011). Medline doi:10.1016/j.bpj.2011.06.010

26. G. Hummer, D. M. Soumpasis, M. Neumann, Computer simulations do not support Cl-Cl pairing in aqueous NaCl solution. *Mol. Phys.* **81**, 1155–1163 (1994). doi:10.1080/00268979400100771

27. C. B. Hübschle, G. M. Sheldrick, B. Dittrich, *ShelXle*: A Qt graphical user interface for *SHELXL*. *J. Appl. Crystallogr.* **44**, 1281–1284 (2011). Medline doi:10.1107/S0021889811043202

28. G. M. Sheldrick, A short history of *SHELX*. *Acta Crystallogr. A* **64**, 112–122 (2008). Medline doi:10.1107/S0108767307043930

29. S. Ye, Y. Li, Y. Jiang, Novel insights into K^+ selectivity from high-resolution structures of an open K^+ channel pore. *Nat. Struct. Mol. Biol.* **17**, 1019–1023 (2010). Medline doi:10.1038/nsmb.1865

30. M. Nishida, M. Cadene, B. T. Chait, R. MacKinnon, Crystal structure of a Kir3.1-prokaryotic Kir channel chimera. *EMBO J.* **26**, 4005–4015 (2007). Medline doi:10.1038/sj.emboj.7601828

31. O. B. Clarke, A. T. Caputo, A. P. Hill, J. I. Vandenberg, B. J. Smith, J. M. Gulbis, Domain reorientation and rotation of an intracellular assembly regulate conduction in Kir potassium channels. *Cell* **141**, 1018–1029 (2010). Medline doi:10.1016/j.cell.2010.05.003

32. M. Iwamoto, S. Oiki, Counting ion and water molecules in a streaming file through the open-filter structure of the K channel. *J. Neurosci.* **31**, 12180–12188 (2011). Medline doi:10.1523/JNEUROSCI.1377-11.2011

33. T. Hoomann, N. Jahnke, A. Horner, S. Keller, P. Pohl, Filter gate closure inhibits ion but not water transport through potassium channels. *Proc. Natl. Acad. Sci. U.S.A.* **110**, 10842–10847 (2013). Medline doi:10.1073/pnas.1304714110

34. S. M. Saparov, P. Pohl, Beyond the diffusion limit: Water flow through the empty bacterial potassium channel. *Proc. Natl. Acad. Sci. U.S.A.* **101**, 4805–4809 (2004). Medline doi:10.1073/pnas.0308309101

35. S. Imai, M. Osawa, K. Takeuchi, I. Shimada, Structural basis underlying the dual gate properties of KcsA. *Proc. Natl. Acad. Sci. U.S.A.* **107**, 6216–6221 (2010). Medline doi:10.1073/pnas.0911270107

36. M. LeMasurier, L. Heginbotham, C. Miller, KcsA: It's a potassium channel. *J. Gen. Physiol.* **118**, 303–314 (2001). Medline doi:10.1085/jgp.118.3.303

37. S. B. Long, X. Tao, E. B. Campbell, R. MacKinnon, Atomic structure of a voltage-dependent K^+ channel in a lipid membrane-like environment. *Nature* **450**, 376–382 (2007). Medline doi:10.1038/nature06265

38. T. Linder, B. L. de Groot, A. Stary-Weinzinger, Probing the energy landscape of activation gating of the bacterial potassium channel KcsA. *PLOS Comput. Biol.* **9**, e1003058 (2013). Medline doi:10.1371/journal.pcbi.1003058

39. S. Bernèche, B. Roux, The ionization state and the conformation of Glu-71 in the KcsA K^+ channel. *Biophys. J.* **82**, 772–780 (2002). Medline doi:10.1016/S0006-3495(02)75439-8

40. V. Hornak, R. Abel, A. Okur, B. Strockbine, A. Roitberg, C. Simmerling, Comparison of multiple Amber force fields and development of improved protein backbone parameters. *Proteins* **65**, 712–725 (2006). Medline doi:10.1002/prot.21123

41. I. S. Joung, T. E. Cheatham 3rd, Determination of alkali and halide monovalent ion parameters for use in explicitly solvated biomolecular simulations. *J. Phys. Chem. B* **112**, 9020–9041 (2008). Medline doi:10.1021/jp8001614

42. L. X. Dang, Mechanism and thermodynamics of ion selectivity in aqueous solutions of 18-crown-6 ether: A molecular dynamics study. *J. Am. Chem. Soc.* **117**, 6954–6960 (1995). doi:10.1021/ja00131a018

43. B. Hess, C. Kutzner, D. van der Spoel, E. Lindahl, GROMACS 4: Algorithms for highly efficient, load-balanced, and scalable molecular simulation. *J. Chem. Theory Comput.* **4**, 435–447 (2008). doi:10.1021/ct700301q

44. T. Darden, D. York, L. Pedersen, Particle mesh Ewald: An N log(N) method for Ewald sums in large systems. *J. Chem. Phys.* **98**, 10089 (1993). doi:10.1063/1.464397

45. U. Essmann, L. Perera, M. L. Berkowitz, T. Darden, H. Lee, L. G. Pedersen, A smooth particle mesh Ewald method. *J. Chem. Phys.* **103**, 8577–8593 (1995). doi:10.1063/1.470117

46. G. Bussi, D. Donadio, M. Parrinello, Canonical sampling through velocity rescaling. *J. Chem. Phys.* **126**, 014101 (2007). Medline doi:10.1063/1.2408420

47. H. J. C. Berendsen, J. P. M. Postma, W. F. van Gunsteren, A. Dinola, J. R. Haak, Molecular dynamics with coupling to an external bath. *J. Chem. Phys.* **81**, 3684–3690 (1984). doi:10.1063/1.448118

48. B. Hess, H. Bekker, H. J. C. Berendsen, J. G. E. M. Fraaije, LINCS: A linear constraint solver for molecular simulations. *J. Comput. Chem.* **18**, 1463–1472 (1997). doi:10.1002/(SICI)1096-987X(199709)18:12<1463::AID-JCC4>3.0.CO;2-H

49. K. A. Feenstra, B. Hess, H. J. C. Berendsen, Improving efficiency of large time-scale molecular dynamics simulations of hydrogen-rich systems. *J. Comput. Chem.* **20**, 786–798 (1999). doi:10.1002/(SICI)1096-987X(199906)20:8<786::AID-JCC5>3.0.CO;2-B

50. J. B. Klauda, R. M. Venable, J. A. Freites, J. W. O'Connor, D. J. Tobias, C. Mondragon-Ramirez, I. Vorobyov, A. D. MacKerell Jr., R. W. Pastor, Update of the CHARMM all-atom additive force field for lipids: Validation on six lipid types. *J. Phys. Chem. B* **114**, 7830–7843 (2010). Medline doi:10.1021/jp101759q

51. B. Roux, S. Bernèche, On the potential functions used in molecular dynamics simulations of ion channels. *Biophys. J.* **82**, 1681–1684 (2002). Medline doi:10.1016/S0006-3495(02)75520-3

52. M. D. Winn, C. C. Ballard, K. D. Cowtan, E. J. Dodson, P. Emsley, P. R. Evans, R. M. Keegan, E. B. Krissinel, A. G. Leslie, A. McCoy, S. J. McNicholas, G. N. Murshudov, N. S. Pannu, E. A. Potterton, H. R. Powell, R. J. Read, A. Vagin, K. S. Wilson, Overview of the *CCP*4 suite and current developments. *Acta Crystallogr. D* **67**, 235–242 (2011). Medline doi:10.1107/S0907444910045749

53. T. Grune, *mtz2sca* and *mtz2hkl*: Facilitated transition from *CCP4* to the *SHELX* program suite. *J. Appl. Crystallogr.* **41**, 217–218 (2008). doi:10.1107/S0021889807050054

54. L. Kissel, R. H. Pratt, Corrections to tabulated anomalous-scattering factors. *Acta Crystallogr. A* **46**, 170–175 (1990). doi:10.1107/S0108767389010718

55. A. T. Brünger, *Methods Enzymol.* **277**, 366–396 (1997).

56. T. Gruene, H. W. Hahn, A. V. Luebben, F. Meilleur, G. M. Sheldrick, Refinement of macromolecular structures against neutron data with *SHELXL2013*. *J. Appl. Crystallogr.* **47**, 462–466 (2014). Medline doi:10.1107/S1600576713027659

57. A. Thorn, G. M. Sheldrick, *ANODE*: Anomalous and heavy-atom density calculation. *J. Appl. Crystallogr.* **44**, 1285–1287 (2011). Medline doi:10.1107/S0021889811041768

58. G. N. Murshudov, P. Skubák, A. A. Lebedev, N. S. Pannu, R. A. Steiner, R. A. Nicholls, M. D. Winn, F. Long, A. A. Vagin, *REFMAC*5 for the refinement of macromolecular crystal structures. *Acta Crystallogr. D* **67**, 355–367 (2011). Medline doi:10.1107/S0907444911001314

59. J. A. Anderson, C. D. Lorenz, A. Travesset, General purpose molecular dynamics simulations fully implemented on graphics processing units. *J. Comput. Phys.* **227**, 5342–5359 (2008). doi:10.1016/j.jcp.2008.01.047

60. HOOMD-blue (http://codeblue.umich.edu/hoomd-blue/index.html).

61. Y. Li, I. Berke, L. Chen, Y. Jiang, Gating and inward rectifying properties of the MthK K^+ channel with and without the gating ring. *J. Gen. Physiol.* **129**, 109–120 (2007). Medline doi:10.1085/jgp.200609655

62. L. Heginbotham, R. MacKinnon, Conduction properties of the cloned Shaker K^+ channel. *Biophys. J.* **65**, 2089–2096 (1993). Medline doi:10.1016/S0006-3495(93)81244-X

63. T. R. Schneider, G. M. Sheldrick, Substructure solution with *SHELXD*. *Acta Crystallogr. D* **58**, 1772–1779 (2002). Medline doi:10.1107/S0907444902011678